Title

Water-soluble chromenylium dyes for shortwave infrared imaging in mice

Permalink

https://escholarship.org/uc/item/08m5t2hv

Journal

Chem, 9(12)

ISSN

2451-9294

Authors

Jia, Shang

Lin, Eric Y.

Mobley, Emily B.
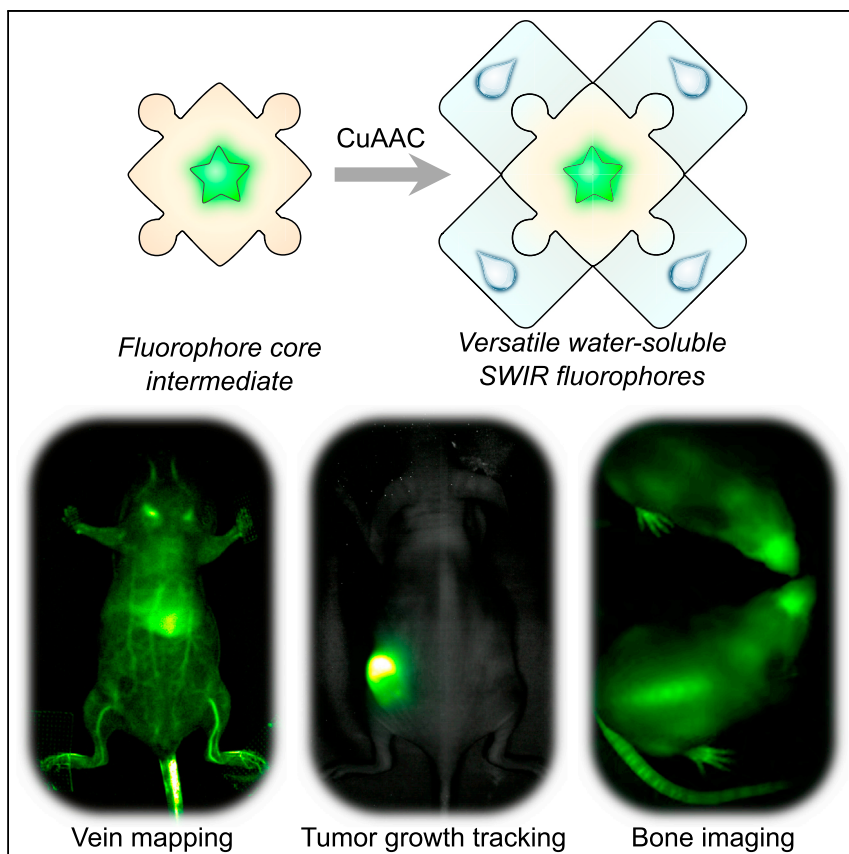
et al.

Publication Date

2023-09-18

Data Availability

The data associated with this publication are in the supplemental files.

Peer reviewed

Chem

Article

Water-soluble chromenylium dyes for shortwave infrared imaging in mice

Fluorophore core intermediate

CuAAC

Versatile water-soluble SWIR fluorophores

Vein mapping   Tumor growth tracking   Bone imaging

Shang Jia, Eric Y. Lin, Emily B. Mobley, ..., Shivakrishna Kallepu, Philip S. Low, Ellen M. Sletten

sletten@chem.ucla.edu

Highlights

Water-soluble, SWIR-emissive chromenylium dyes for carrier-free *in vivo* imaging

Late-stage modification provides modular scaffold for tuning solubility and activity

Tetra-ammonium dye enables tracking of the growth of pre-stained tumors for >5 weeks

Tetra-phosphonate dye enables visualization of bones in anesthetized and awake mice

The development of small-molecule shortwave infrared (SWIR, 1,000–2,000 nm) fluorophores for *in vivo* imaging has recently exploded; however, most SWIR-emissive fluorophores are hydrophobic. Here, we performed late-stage functionalization of a chromenylium heptamethine dye to introduce aqueous solubility and/or bioactivity. With a modular synthesis, we accessed a panel of bright and water-soluble SWIR fluorophores, enabling SWIR imaging of veins, tumor growth, and bones. This versatile design provides an avenue for modular construction of water-soluble SWIR fluorophores.

3 GOOD HEALTH AND WELL-BEING

Article

Water-soluble chromenylium dyes for shortwave infrared imaging in mice

Shang Jia,[1,4] Eric Y. Lin,[1] Emily B. Mobley,[1] Irene Lim,[1] Lei Guo,[2,5] Shivakrishna Kallepu,[3] Philip S. Low,[3] and Ellen M. Sletten[1,6,*]

SUMMARY

In vivo imaging using shortwave infrared (SWIR) light (1,000–2,000 nm) benefits from deeper penetration and higher resolution compared with using visible and near-infrared wavelengths. However, the development of biocompatible SWIR contrast agents remains challenging. Despite recent advancements, small-molecule SWIR fluorophores are often hindered by their significant hydrophobicity. We report a platform for generating a panel of soluble and functional dyes for SWIR imaging by late-stage functionalization of a versatile fluorophore intermediate, affording water-soluble dyes with bright SWIR fluorescence in serum. Specifically, a tetra-sulfonate derivative enables clear video-rate imaging of vasculature with only 0.05 nmol dye, and a tetra-ammonium dye shows strong cellular retention for tracking of tumor growth. Additionally, incorporation of phosphonate functionality enables imaging of bones in awake mice. This modular design provides insights into facile derivatization of existing SWIR fluorophores to introduce both solubility and bioactivity toward *in vivo* bioimaging.

INTRODUCTION

Optical imaging utilizing shortwave infrared (SWIR) light (1,000–2,000 nm; also referred to as second Near-Infrared Region [NIR-II]; Figure 1A) is a rapidly growing research area.[1–3] These long-wavelength photons benefit from reduced scattering, tissue absorption, and autofluorescence compared with visible (400–700 nm) and NIR (700–1,000 nm) light.[4–7] These qualities render the SWIR region well-suited to assist research in small model animals and expand the scope of optical clinical diagnostics. Indeed, in 2020, 11 years after the seminal report of SWIR imaging in mice,[8] a study in humans concluded that SWIR detection was superior to NIR detection in image-guided surgery with higher tumor detection sensitivity and increased signal-to-noise ratio.[9] The clinical trial employed indocyanine green (**ICG**, Figure 1B), a U.S. Food and Drug Administration (FDA)-approved NIR fluorophore with a small percentage of emission in the SWIR region, as a contrast agent for their studies. If bright, SWIR analogs of **ICG** were available, the benefits of SWIR detection would be more pronounced for these surgical guidance procedures in terms of sensitivity and accuracy. Additionally, water-soluble SWIR fluorophores will expand the scope of experiments that can be performed in model organisms.[10]

ICG is a heptamethine dye with benzo[e]indolium heterocycles (Figure 1B). Polymethine dyes have significant advantages as optical contrast agents including small size, biocompatibility, and excellent absorption properties (narrow absorption bands with high absorbance coefficients [ε]).[11,12] Consequently, polymethine dyes

THE BIGGER PICTURE

Optical imaging is a safe, rapid, and low-cost imaging modality for (pre)clinical applications; however, it suffers from low penetration of light through tissue. Moving to longer wavelengths such as the shortwave infrared (SWIR) region increases the penetration depth, which has resulted in significant efforts to develop biocompatible, small-molecule SWIR fluorophores. Numerous fluorophores have been developed, but most are too hydrophobic to be used without a delivery agent.

Here, we report a series of water-soluble SWIR fluorophores that can be visualized in mice. Modification with different moieties brings distinct properties that enable the imaging of veins, bones, or tumor growth in mice. This modular and facile synthesis renders one hydrophobic SWIR fluorophore core applicable to diverse applications, providing insights into future construction of functional SWIR fluorophores for *in vivo* imaging.
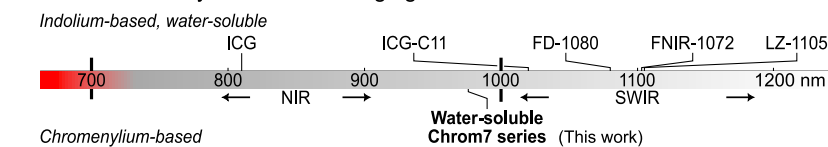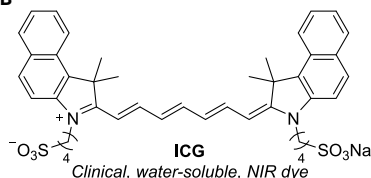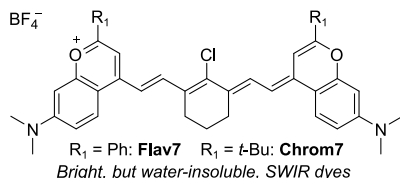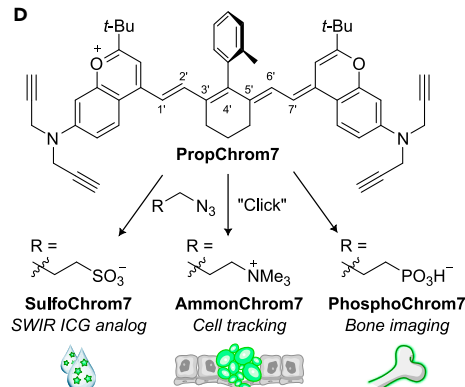
Figure 1. Design of hydrophilic and versatile Chrom7 derivatives
(A) Water-soluble polymethine dyes used for SWIR imaging and their emission wavelengths.
(B) Structure of **ICG**.
(C) Structures of **Flav7** and **Chrom7**.
(D) Derivatization of **PropChrom7** into a series of water-soluble and functional SWIR imaging agents.

have seen considerable success as water-soluble probes and fluorophores in the visible and NIR regions.[13–15] Over the past 5 years, numerous SWIR-emissive poly-methine dyes have been prepared using two red-shifting strategies: polymethine chain extension[16,17] or heterocycle modification.[18–20] Although each of these approaches has been successful at producing fluorophores with excellent photophysical properties for the SWIR region in organic solvents, there are significant challenges in solubilizing these large, planar, aggregation-prone fluorophores in water. Polymethine chain extension is the most classic method to red-shift this class of fluorophores, but as the chain lengths are increased, the delocalization of the π bonds across the polymethine chain can become compromised, leading to a molecule with poly-ene character that has unfavorable photophysical properties. This phenomenon is termed ground-state desymmetrization and leads to broadened absorption bands with decreased absorbance coefficients and lowered quantum yields of fluorescence.[21,22] Ground-state desymmetrization is enhanced in polar aqueous media,[22] rendering imaging of long chain polymethine dyes in physiological conditions more challenging. Heterocycle modification allows for SWIR fluorophores with pentamethine or heptamethine chains, decreasing contributions from ground-state desymmetrization; however, these heterocycles are often more hydrophobic than the classic indolium heterocycles, and the approaches commonly used to solubilize polymethine dyes in water are not successful on these more customized heterocycles. In fact, the small number of water-soluble polymethine SWIR fluorophores to date all include indolium-derived heterocycles with polymethine chain extension, and varying amounts of ground-state desymmetrization are observed in water (Figures 1A and S1).[16,17,23,24]

Here, we report a modular approach toward water-soluble SWIR-emissive chromenylium heptamethine dyes. The chromenylium heterocycle scaffold is a bright, red-shifted heterocycle for polymethine fluorophores (e.g., **Flav7** and **Chrom7**, Figure 1C).[25–31] Chromenylium polymethines encapsulated in micelles have enabled SWIR imaging at record frame rates,[25–27] with multiple channels,[26,27] and have been incorporated in responsive fluorescence resonance energy transfer (FRET) probes.[30] To render the chromenylium heptamethine dyes water-soluble, we determined that the following two critical modifications are necessary: steric bulk on the polymethine linker to block π-π stacking and addition of multiple charged

[1]Department of Chemistry and Biochemistry, University of California, Los Angeles, Los Angeles, CA 90095, USA

[2]Linde-Robinson Laboratories, California Institute of Technology, Pasadena, CA 91125, USA

[3]Department of Chemistry, Purdue University, West Lafayette, IN 47907, USA

[4]Present address: Department of Chemistry and Biochemistry, University of Arkansas, Fayetteville, Fayetteville, AR 72701, USA

[5]Present address: Department of Civil Engineering, University of Arkansas, Fayetteville, Fayetteville, AR 72701, USA

[6]Lead contact

*Correspondence: sletten@chem.ucla.edu
https://doi.org/10.1016/j.chempr.2023.08.021

functionalities to impart sufficient water solubility. We prepare the clickable hydrophobic fluorophore **PropChrom7** (Figure 1D), which contains an *ortho*-methyl substituted phenyl group at the 4'-position to prevent aggregation and four propargyl groups for copper-catalyzed azide-alkyne cycloaddition (CuAAC) with charged azides to introduce hydrophilicity and/or functionality into the final products. **PropChrom7** is a versatile intermediate for the preparation of a range of SWIR fluorophores with different functional groups and charge states. Using this approach, we obtained a panel of water-soluble **Chrom7** derivatives that carry sulfonates (**SulfoChrom7**), ammoniums (**AmmonChrom7**), and zwitterions (**ZwitChrom7**) with varying localization properties (Figure 1D). These dyes all show monomeric dispersion in serum at dilute conditions with bright SWIR fluorescence. Notably, negatively charged **SulfoChrom7** shows slow absorption by tissue which allows for imaging of superficial veins with low detection limits; quintuply positively charged **AmmonChrom7** shows efficient uptake and prolonged retention in cells, enabling tracking of xenograft tumor growth in mouse models. We further showcased this late-stage functionalization design by incorporation of tetravalent phosphonates as both hydrophilic groups and calcium-binding sites to achieve high-resolution bone imaging in both anesthetized and moving mice. We expect that our platform will expand to provide water-soluble SWIR fluorophores with varying photophysical properties and more bioactivity, as well as inspire more SWIR fluorophores packaged as modular building blocks to furnish complex animal imaging tools.

RESULTS AND DISCUSSION

Design and synthesis of water-soluble SWIR heptamethine dyes

When considering how to prepare water-soluble derivatives of chromenylium SWIR dyes, we aimed to design a synthesis that would minimize water-soluble intermediates and maximize diversity of the final fluorophores. We focused on first installing aggregation-minimizing functionalities on a hydrophobic scaffold that could then be transformed into a water-soluble fluorophore through a click reaction with a charged functionality. To disfavor aggregation, we base our fluorophore on **Chrom7** as its bulky di-*tert*-butyl substitution acts as a steric hindrance that disfavors aggregation compared with planar **Flav7**, as evidenced by their absorption profiles in micelle formulations.[25,27] However, the two *tert*-butyl groups were not effective enough at reducing aggregation, and an *ortho*-methylphenyl group was installed at the 4' position of the polymethine chain. This substitution is analogous to the pendent aryl ring in Tokyo Green.[32] Due to its steric demands, the 4'-substitution is perpendicular to the dye plane, which positions its protruding methyl group close to the polymethine bridge, thus preventing another dye molecule from effective π-π stacking necessary for aggregation to occur. These aggregation-minimizing features were consolidated into a tetra-propargylated chromenylium fluorophore, deemed **PropChrom7**. To promote the aqueous solvation of the fluorophores, we introduced hydrophilicity at the very last step, where we performed CuAAC between **PropChrom7** and selected hydrophilic azides. The four equivalents of hydrophiles are expected to render the heptamethine dyes water soluble. Initially, we selected organic azides carrying sulfonate, ammonium, or zwitterion functionality.

PropChrom7 as a central building block enables the facile synthesis of the water-soluble dyes in this work. The synthesis of **PropChrom7** is carried out in organic solvents similar to previously reported chromenylium dyes. It is only in the last step converting **PropChrom7** to the final water-soluble fluorophore where aqueous solvent and high-performance liquid chromatography (HPLC) separation were necessary (Scheme 1). Specifically, we obtained chromone **1** from the microwave-assisted
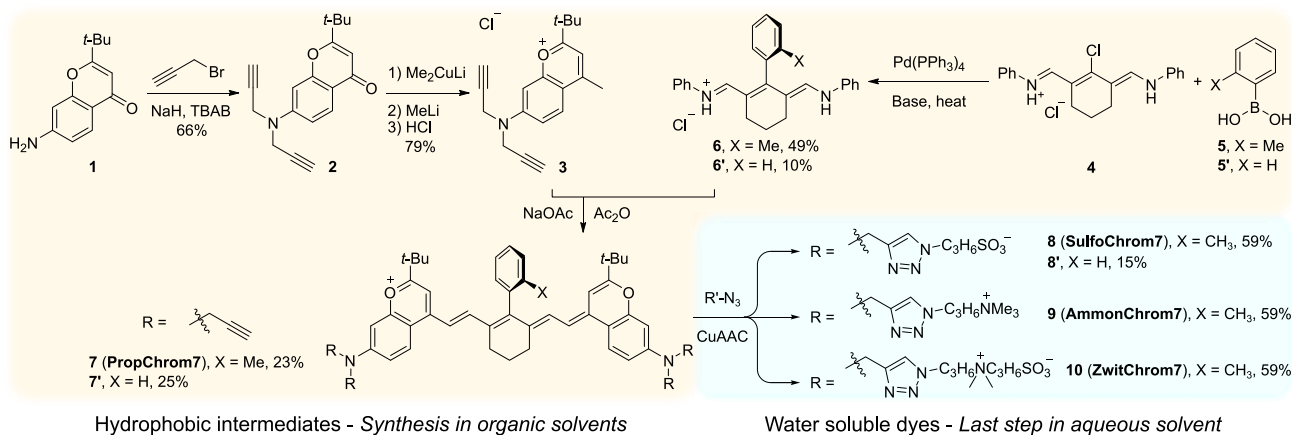
Scheme 1. Synthesis of PropChrom7 and post-synthetic CuAACs to afford SulfoChrom7, AmmonChrom7, ZwitChrom7, as well as the control dye (8′) without *o*-methyl substitution

pyrone synthesis,[33] utilizing allyl protecting groups on the aniline that were compatible with the high temperatures and pressures encountered in microwave synthesis (supplemental experimental procedures). Following allyl group deprotection with $Pd(PPh_3)_4$, chromone **1** was obtained, and the propargyl substituents were installed by treatment with propargyl bromide to yield **2**. The standard conditions for conversion of chromones to chromenylium dyes using MeMgBr or MeLi both gave poor yields due to reactivity with the propargyl groups. We found that pre-treatment with Me_2CuLi provided an *in situ* protection of the terminal alkynes, allowing isolation of **3** in 79% yield. In parallel to the synthesis of propargylated chromenylium **3**, we prepared polymethine linker **6**, which contains the aggregation-blocking *o*-methyl-phenyl group. Linker **6** was constructed from Suzuki-Miyaura cross-coupling between commercially available compounds **4** and **5** at 120 °C, which is harsher than the commonly used conditions for this type of conversion[34] to compensate for the increased steric demands. **PropChrom7 (7)** was prepared from the condensation of **6** and **3** in 23% yield. This central intermediate then underwent CuAAC with hydrophilic organic azides under a commonly used condition for bioconjugation with tris-hydroxypropyltriazolylmethylamine (THPTA) as the ligand,[35] but in a 1:2 mixture of water and methanol, to accommodate the solubility of both the hydrophobic dye and hydrophilic azide. This procedure resulted in **8 (Sulfo-Chrom7)**, **9 (AmmonChrom7)**, and **10 (ZwitChrom7)** all with ca. 59% yield.

In vitro characterization of water-soluble SWIR fluorophores

We first tested the photophysical behaviors of the dyes in different conditions (Figures 2A and S8A). All three hydrophilic dyes (**Sulfo-, Ammon-,** and **Zwit-Chrom7**) and hydrophobic dye **PropChrom7** show monomeric dispersion in MeOH and can be compared directly (Figures 2A and S2–S5). By converting the propargyl groups on **PropChrom7** to the triazolylmethyl groups, the fluorophore exhibits a 10 nm red-shift in absorption and a 16 nm red-shift in emission maxima, corresponding to the increased electron donation from the triazoles (Figures 2A, 2D, and S2–S5). Most importantly, all the hydrophilic dyes exhibit similar properties in absorption maximum and extinction coefficient, as well as fluorescent quantum yield (Figures 2A, 2D, and 2E), suggesting that the functionality appended to **Prop-Chrom7** can be varied without compromising the photophysical properties.

Owing to the structural homology of **8–10**, we are able to compare the water-solubilizing ability of sulfonate, ammonium, and zwitterion functionalities. As shown in

A

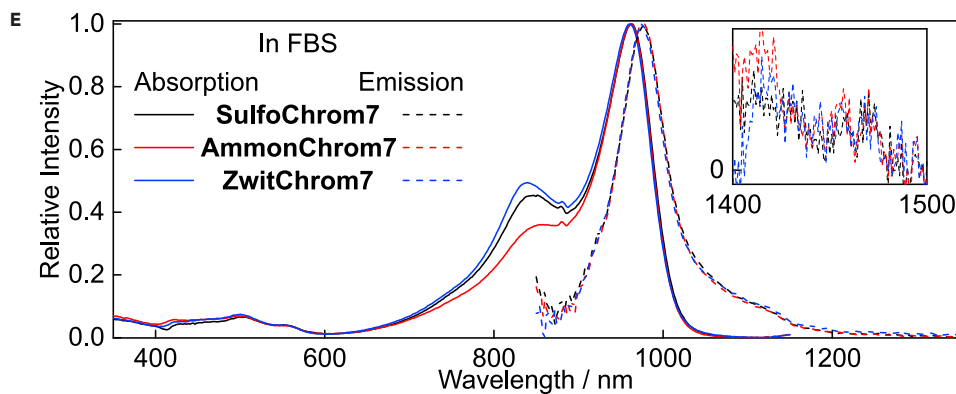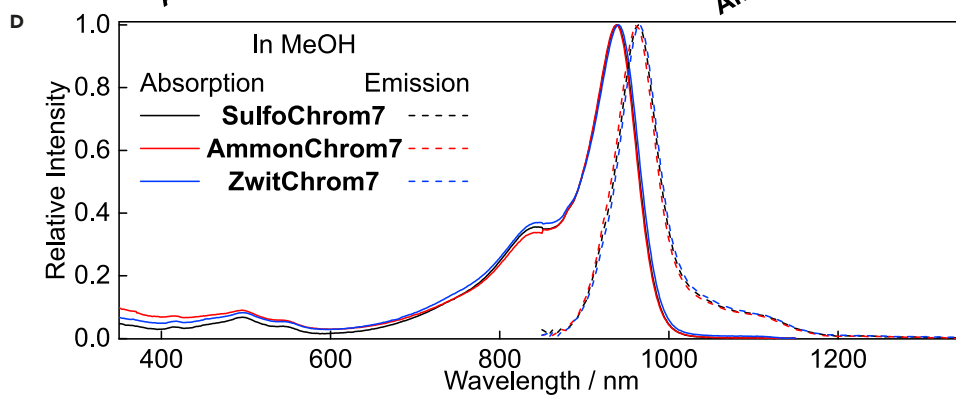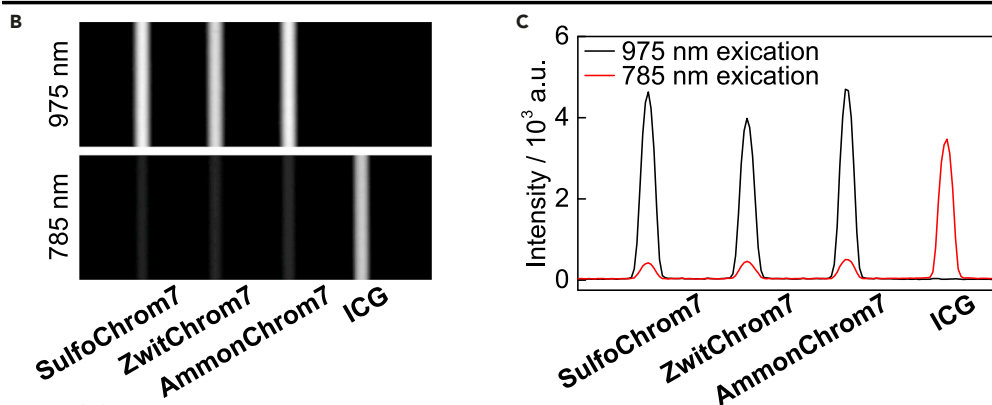| Fluorophore	Solvent	$\lambda_{max, abs}$ / nm	ε_{max} / 10^4 M^{-1}cm^{-1}	$\lambda_{max, ems}$ / nm	Φ_F / %
PropChrom7	MeOH	928	14	946	1.18
SulfoChrom7	MeOH	938	16.5	964	1.06
	H_2O	923[a]	2.4[a]	941	n.d.[b]
	FBS	963	9.5	976	0.56
AmmonChrom7	MeOH	938	16	962	1.18
	H_2O	923	6.2	940	0.43
	FBS	962	11	977	0.58
ZwitChrom7	MeOH	940	16.4	965	1.01
	H_2O	ca. 923[a]	2.1[a]	940	n.d.[b]
	FBS	960	11.5	975	0.32

B

C

D

E

Figure 2. Photophysical comparisons of water-soluble SWIR fluorophores

(A) Table of photophysical properties. See Figure S8A for error values.

[a]Peak at the second maximum absorption (monomer absorption). [b]Not determined due to strong aggregation.

(B) Brightness comparison by SWIR imaging of each water-soluble dye (2 µM) in FBS in capillaries under 975 nm illumination (100 mW/cm^2), with 2 µM of ICG in FBS under 785 nm illumination (50 mW/cm^2) as a benchmark (1,100 nm long-pass filter, 4 ms/frame).

(C) Quantification of (B).

(D and E) Overlay of absorption (solid line) and emission (dotted line) spectra of 2 µM Sulfo-, Ammon-, or Zwit-Chrom7 in methanol (D) or FBS (E). Zoomed-in emission spectra in FBS between 1,400 and 1,500 nm are shown as inset in (E).

the absorption spectrum in H$_2$O, ammonium salt possesses the strongest ability to solubilize the chromenylium fluorophore as evidenced by the dominant monomeric absorption profile of **AmmonChrom7** at concentrations as high as 2 µM (Figures S4B and S4D). Next best is the sulfonate group in **SulfoChrom7**, which shows a discernible monomer absorption (Figures S3B and S3D), whereas the zwitterionic moiety in **ZwitChrom7** is primarily aggregated in water (Figures S5B and S5D). Although the dyes do display some aggregation in water, gratifyingly, there is minimal evidence of ground-state desymmetrization in H$_2$O, suggesting an advantage of heptamethine SWIR dyes (Figure S8D).

Next, we evaluated the fluorophores in more biologically relevant fetal bovine serum (FBS) and found that all three fluorophores displayed a well-defined monomeric absorption and emission characteristic of polymethine dyes (Figure 2E). **AmmonChrom7** aggregates the least in FBS with monomeric absorption observed up to 32 µM, whereas **SulfoChrom7** and **ZwitChrom7** have dominant monomeric absorption up to 8 µM. Additionally, in FBS, the absorbance of the three dyes was red-shifted by ca. 40 nm (Figure 2E). These observations suggest that all three fluorophores are interacting with serum proteins, which is a behavior similar to that seen in **ICG**.[36] The quantum yield values for **AmmonChrom7** and **SulfoChrom7** are above 0.5% in FBS, a notable metric for SWIR dyes in aqueous media. **ZwitChrom7** is slightly lower at 0.32% in FBS. Although these quantum efficiencies are lower than those in methanol, or the parent **Chrom7** scaffold in dichloromethane, it should be noted that SWIR emissions are typically greatly reduced in water with quenching by abundant energy-matched O–H vibrations and overtones.[37,38] Nonetheless, comparative capillary images in FBS between **AmmonChrom7**, **SulfoChrom7**, **ZwitChrom7**, and **ICG** with 785 or 975 nm excitation suggest that all three SWIR dyes are comparable with or superior to **ICG** for SWIR imaging (Figures 2B and 2C).

We additionally sought to evaluate the role of the *o*-methyl in minimizing aggregation due to the additional steric bulk at the 4′-position. Toward this end, we prepared **8′** as an analog of **SulfoChrom7** that contains only a phenyl substitution at this 4′-site (Scheme 1) and compared the photophysical properties of **8′** and **SulfoChrom7** in different media (Figure S6). Although the monomer peak of **8′** shows similar absorption and emission maxima to that of **SulfoChrom7** in methanol (Figures S6B and S8A), drastically different behavior is observed in water and FBS. **SulfoChrom7** is primarily monomeric in FBS, whereas **8′** displays significant aggregation (Figures S6D, S6F, and S6G), and in water, the monomer peak is barely detectable for **8′** (Figures S6C, S6E, and S6H). These photophysical observations indicate that *o*-methyl group is important for minimizing aggregation in this family of SWIR fluorophores.

We further tested the dyes for their stability in *in vitro* assays. Although these hydrophilic dyes exhibit gradual degradation in both water and FBS in the dark similar to the behavior of ICG,[39,40] such behavior is greatly inhibited with the addition of glutathione (GSH) in the millimolar range as a mimic of the reductive cellular context

(Figures S7F–S7H). In fact, contrary to some other heptamethine dyes that are prone toward nucleophilic degradation from thiols,[41] **SulfoChrom7** and **ZwitChrom7** exhibit negligible reactivity toward GSH in FBS, as suggested by the retention of both the absorption intensity and the max absorption wavelength in the presence of 15 mM GSH (Figures S7F and S7H). Instead, the major degradation pathway of these dyes in water is attributed to oxidation of the fluorophore, as evidenced by the increase of 16 (1 oxygen atom) or 32 amu (2 oxygen atoms) on the degradation products (Figures S7A–S7E). These pathways may explain the protection effect of GSH, as the reducing environment can possibly inhibit the oxidative degradation of the fluorophores.[42] Furthermore, their photobleaching rates in FBS are in the same magnitude as the parent **Chrom7** fluorophore in DMSO[27] (Figure S8B). Also noteworthy is that **8′**, the **SulfoChrom7** analog that lacks the *o*-methyl group on the 4′-aryl substitution, shows substantial amount of immediate oxidative degradation when dissolved in water (Figures S6C, S6E, and S6H), which is suggestive that the steric hindrance from the *o*-methyl group may enhance the kinetic stability of this family of dyes.

We also evaluated the cytotoxicity of these dyes by MTT assay. Inhibition of proliferation in HEK293 cells is minimal for **AmmonChrom7** even with dye concentrations as high as 100 μM over 18 h, and the growth inhibition of **SulfoChrom7** and **AmmonChrom7** are also mild at 20 μM (<15% inhibition, Figure S8C). As such, we deem these dyes suitable for use in animals at or below ca. 10 μM (20 nmol injection for 5 weeks or older mice) concentrations.

Biodistribution of water-soluble SWIR fluorophores

After *in vitro* characterization, we carried out *in vivo* imaging of the three hydrophilic dyes in mice to compare the differences in biodistribution. Toward this end, we injected 20 nmol of each dye into the tail vein and observed a strong fluorescence signal for each dye which allowed imaging at 100 frames per second (fps, 0.5–2 ms exposure time, Figures S9–S11) through an 1,100 nm long-pass (LP) filter. All three dyes initially localized primarily in the liver and vasculature. After 3 h, almost all **AmmonChrom7** accumulated in the liver (Figures S10A–S10D), whereas **SulfoChrom7** and **ZwitChrom7** showed diffuse signal through the mouse body but still with substantial liver accumulation (Figures S9A–S9D and S11A–S11D). The distribution of all three dyes remained relatively unchanged over 2 days, whereas their brightness decreased slightly in the mouse body and in the liver (Figures S9G, S9H, S10G, S10H, S11G, and S11H), indicating their relatively slow secretion or metabolism. In fact, their lasting fluorescence signals were retained much beyond their half-life in aerated FBS, suggesting significantly reduced degradation *in vivo*. Dissection of the organs 48 h after injection revealed that all the dyes stained primarily the liver (Figures S9E, S9F, S10E, S10F, S11E, and S11F). Although **AmmonChrom7** displayed the strongest accumulation in the liver as noted, all three dyes showed some staining in the kidney and intestine, suggesting slow clearance through these pathways. Compared with **ICG**, which has a blood $t_{1/2}$ of 10 min[43] followed by hepatobiliary clearance within 6 h,[24,44] the lasting *in vivo* fluorescence of our dyes offers a valuable reference for the future development of SWIR contrast agents. The slower pharmacokinetics may enable flexible introduction time before clinical imaging. The long circulation time of these fluorophores also makes them ideal for long-term tracking of biological events in living mice for research purposes.

Systemic imaging with SulfoChrom7

The anionic **SulfoChrom7** is the most similar of the fluorophores to **ICG**, the current benchmark for untargeted optical *in vivo* imaging, and appeared the brightest of the fluorophores in capillary imaging experiments (Figure 2B). For these reasons, we
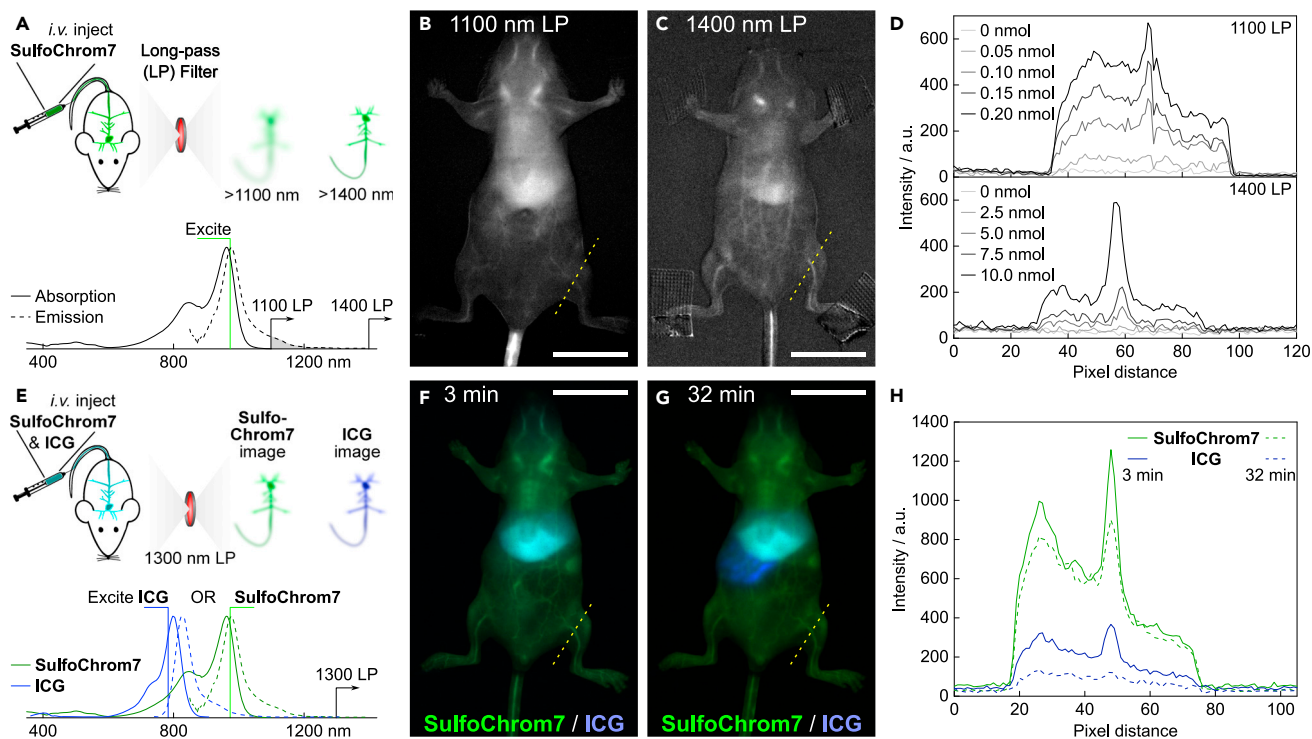
Figure 3. Video-rate imaging of mouse vasculature with _i.v._ injected SulfoChrom7

(A) Schematics of _i.v._ injection of **SulfoChrom7** for vasculature imaging under different filters.

(B–D) Fluorescence images of mice recorded at 30 ms/frame (B) under 1,100 nm LP filter with 0.05 nmol dye injected as a 50 µL solution (20 frames averaged, max brightness 646 excluding tail region), or (C) under 1,400 nm LP filter with 5.0 nmol dye injected as a 100 µL solution (20 frames averaged, max brightness 289 excluding tail region); their raw brightness profiles along the highlighted line is shown in (D). See Videos S1 and S2 for injection video.

(E) Schematics of co-injection of **SulfoChrom7** and **ICG** for their direct comparison under two-channel imaging.

(F–H) Fluorescent images of a mouse at 10 ms/frame under 1,300 nm LP filter (F) 3 min (84 frames averaged, max brightness 4,302 [green] and 3,960 [blue]) or (G) 32 min (87 frames averaged, max brightness 3,692 [green] and 4,027 [blue]) after _i.v._ injection of **SulfoChrom7** (10 nmol, shown in green) and **ICG** (10 nmol, shown in blue); their raw brightness profiles along the highlighted line is shown in (H). Illumination was provided at 100 mW/cm^2 for 975 nm and 50 mW/cm^2 for 785 mm. Scale bars: 2 cm.

performed a more extensive set of _in vivo_ imaging experiments with **SulfoChrom7** to determine its limit of detection and performance in comparison with **ICG**. Current clinics usually apply 2.5 mg (ca. 0.05 µmol/kg) **ICG** for detection of lymph nodes, tumors, and vital structures under routine NIR imaging,[45] whereas for SWIR imaging, a much larger dose of **ICG** is required to compensate for the small fraction of the SWIR emission from **ICG** (0.3 or 0.6 µmol/kg in mouse, pig, or human) but still with >100 ms exposure time.[9,24,44,46] Considering that **SulfoChrom7** is a bright fluorophore with the majority of its emission in the SWIR, we anticipate that a very small dose of **SulfoChrom7** is necessary for SWIR imaging. This represents an advance over **ICG**, since it is beneficial to introduce as little contrast agent as possible to minimize unnatural interactions and toxicity. To determine the relevant concentrations necessary for SWIR imaging with **SulfoChrom7**, we performed sequential tail vein injections of 0.05 nmol (ca. 2.5 nmol/kg) of **SulfoChrom7**. We set our desired imaging parameters at 33 fps (real-time imaging) first with an 1,100 nm LP filter (Figure 3A). As soon as the first dose of 0.05 nmol dye was introduced, the liver lit up together with discernible saphenous and medial marginal veins, facial veins, and abdominal wall veins (Figures 3B and 3D). As more dye was injected, the signal increased in a dose-dependent manner, giving rise to a higher signal-to-noise ratio (Figures 3D and S12A–S12F; Video S1). This is, to the best of our knowledge, the smallest

amount of dye directly administered without formulation to enable high-quality video-frame rate non-invasive imaging.

We then performed a similar set of experiments with more restrictive imaging metrics of 33 fps and a 1,400 LP filter. Water molecules have considerable absorption of light beyond 1,400 nm, which reduces signal from deeper tissue and simultaneously enhances the resolution by attenuating scattered light (Figure 3A).[47] For these experiments, we increased the amount of dye injected to 4 × 2.5 nmol to compensate for the reduced integrated signal after 1,400 nm (Figure 2E) as well as the signal loss from water absorption. After 5.0 nmol dye was introduced, the fluorescence image clearly delineated a map of the vasculature system of the mouse, whereas the interference from liver accumulation was reduced due to the more significant depth of the liver (Figures 3C and 3D). As the amount of dye was increased, fluorescence signals increased with a more distinct vein map and reduced noise level (Figures 3D and S12G–S12L; Video S2). With 10 nmol **SulfoChrom7**, we were able to obtain a detailed image of the vasculature with minimal noise level (Figure S12J). On the other hand, although **ICG** also lit up the vein system, the contrast was much weaker than **SulfoChrom7** under the same settings because of the small emission tail at 1,100 nm or longer wavelengths for SWIR imaging. Moreover, the observation window is much shorter, which we further assessed in the next step where we performed a direct comparison of **SulfoChrom7** and **ICG** for vasculature imaging.

We are able to directly compare **ICG** and **SulfoChrom7** as SWIR contrast agents in the same mouse because they can be selectively excited at different wavelengths (Figure 3E, 785 nm for **ICG**, and 975 nm for **SulfoChrom7**). For these experiments, we used a 1,300 LP filter to compromise between resolution and signal intensity. As shown in the fluorescence image, immediately after injection, both dyes stained the vasculature with much stronger signal in the **SulfoChrom7** channel owing to its red-shifted emission (Figures 3F and 3H). Within 30 min, most **ICG** accumulated in the liver with secretion into the intestine, leaving negligible signal in the mouse body, whereas **SulfoChrom7** still reflected the superficial vasculature map while also displaying liver accumulation (Figures 3G and 3H). **SulfoChrom7** displayed an increasing brightness ratio over **ICG** in veins over time (up to 7- to 8-fold, Figures S13E–S13H). A similar trend is also displayed when imaging with 1,100 or 1,400 nm LP filter, where signals from **SulfoChrom7** are retained in vasculature during the 33 min time frame, whereas **ICG** clears into the liver and intestines (Figures S13A–S13D and S13I–S13L). Taken together, **SulfoChrom7** benefits from its higher SWIR brightness and longer blood circulation time than **ICG**, suggesting itself as an excellent SWIR fluorophore to visualize the superficial vein system over long periods of time with high sensitivity and adjustable resolution in different imaging setups.

Tracking of tumor growth with AmmonChrom7

Next, we explored the utility of the highly cationic **AmmonChrom7** fluorophore. **AmmonChrom7** features a permanent $z = +5$ and m/z of 269.6. This high charge density is close to that of some cell-penetrating peptides (e.g., nonaarginine $m/z = 159$ at $z = 8$, transactivator of transcription [TAT] peptide peptide $m/z = 233$ at $z = 7$), suggesting its effective internalization into cells. Highly cationic dye molecules have also shown effective cellular uptake and find utility in cell-tracking applications,[48,49] whereas many positively charged nanoparticles have been developed for such purpose.[50] We thus anticipated that **AmmonChrom7** could be similarly internalized into cells for long-term visualization (Figure 4A). To test this hypothesis, we incubated HEK293 cells with 50 μM of **AmmonChrom7**, **SulfoChrom7**, and **ZwitChrom7** and
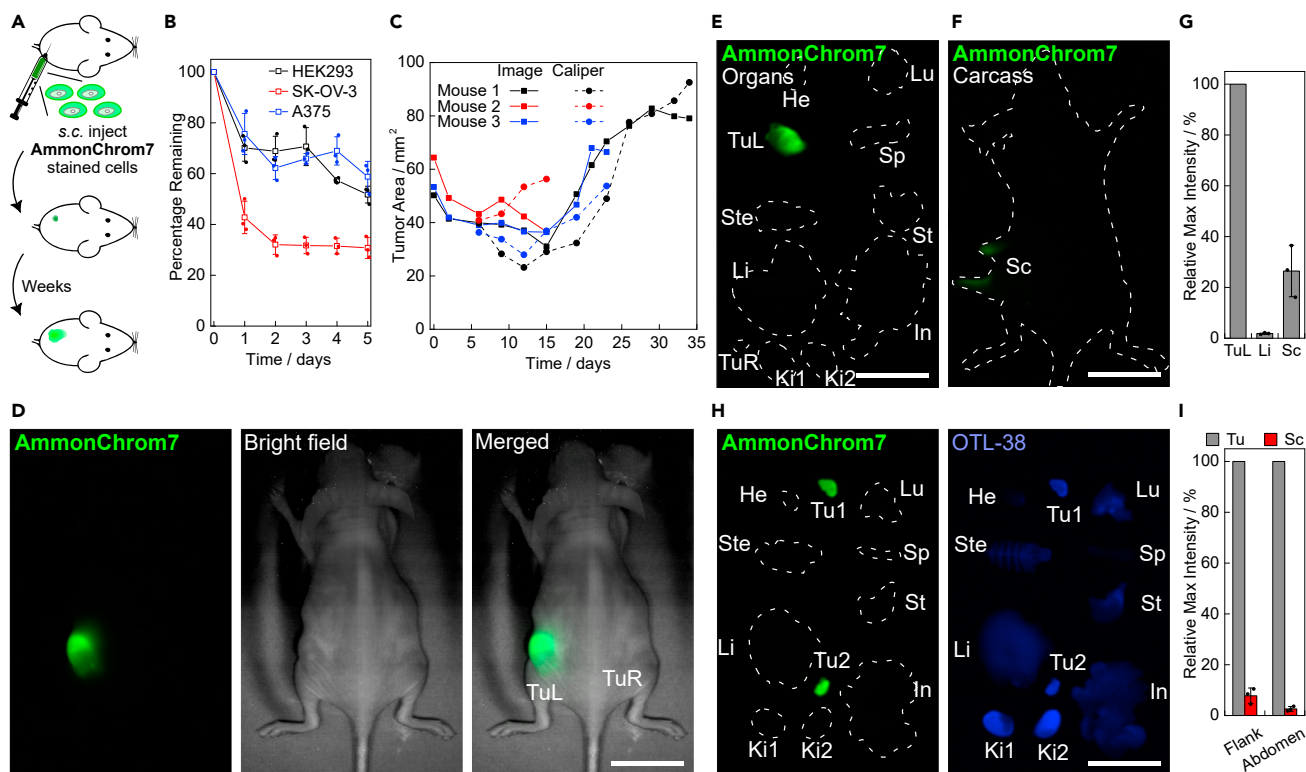
Figure 4. Tracking of tumor growth using AmmonChrom7

(A) Schematics of *s.c.* injection of **AmmonChrom7** stained cells for tracking of their *in vivo* growth.

(B) Uptake and retention of **AmmonChrom7** in different cell lines.

(C) Comparison of the growth curves of stained A375 as determined by fluorescence imaging and caliper measurement in three mice.

(D) *In vivo* images of A375 tumors 34 days after xenograft on mouse 1 (1 ms/frame, 31 frames averaged, max brightness 7,957).

(E and F) *Ex vivo* fluorescent images of A375 tumors and organs (E) and carcass (F) of mouse 1 34 days after xenograft (0.8 ms/frame, 51 frames averaged, max brightness 10,873, E and 2,920, F). See Figures S16E and S16F for corresponding bright-field images. Lu, lung; Sp, spleen; St, stomach; In, intestine; He, heart; Ste, sternum; Li, liver; Ki, kidney; TuL, left, stained tumor; TuR, right, unstained tumor; Sc, subcutaneous tissue around TuL.

(G) Maximum brightness of *ex vivo* fluorescent tumor, liver, and subcutaneous tissue surrounding the tumor (mean ± SD, mouse 1: 34 days, mouse 2: 15 days, mouse 3: 23 days after xenograft).

(H) *Ex vivo* fluorescent images of SK-OV-3 tumors and organs 39 days after xenograft and 4 h after *i.v.* injection of OTL-38 (1 ms/frame, 112 frames averaged, max brightness 9,928 [green] and 2,095 [blue]). See Figure S17G for corresponding bright-field image. Tu1, abdomen *s.c.* tumor; Tu2, flank *s.c.* tumor.

(i) Maximum fluorescence intensity of *ex vivo* tumors and their surrounding hypodermis after tumor removal from the sacrificed mice (n = 3, mean ± SD), 39 days after xenograft. Illumination was provided at 100 mW/cm^2 for 975 nm and 50 mW/cm^2 for 785 mm. Scale bars: 2 cm.

analyzed the absorbance of cell lysates over time. We found significant absorbance for cells treated with **AmmonChrom7**, whereas the signal for **SulfoChrom7** and **ZwitChrom7** is minimal (Figures S14A and S14B). The cellular labeling of **AmmonChrom7** dropped significantly on the first day after staining, possibly due to exocytosis from the saturated cytosol, and then decreased fairly slowly to retain a signal around 50%–70% of the initial brightness over 5 days (Figure 4B). Similar behavior was also observed in A375 cells, a human melanoma cell line, and SK-OV-3 cells, a human ovarian cancer cell line (Figure 4B). We further tested the retention of **AmmonChrom7** using RAW 264.7 cells. The emission from **AmmonChrom7** is determined to originate from the monomeric form in both free solution and in loaded cells, as supported by the little emission from excitation of the blue-shifted aggregate peak at a high concentration in water (10 μM, Figure S15A) and the minimal aggregation in treated cells (Figure S15B). Adhered cells were readily visualized under the SWIR camera in a 12-well plate 2 weeks after treatment with

AmmonChrom7 (Figure S15C). Some signal loss was observed over 7 days, which we primarily attribute to FBS starvation-induced cell death rather than the loss of cellular dye content (Figures S15D–S15F). In fact, the days to weeks of persistent signal from **AmmonChrom7** well exceeds the half-life of the dye in FBS or water, which is indicative of the protective effects from the reductive cellular environment and the interaction with the cellular proteome. Besides the enhanced stability in cells, **AmmonChrom7** staining allows for sensitive detection of cells in model animals, where we were able to observe as little as 1.4×10^4 freshly stained RAW 264.7 cells when placed at the heart of a synthetic mouse phantom under the SWIR camera over an 1,100 nm LP filter (Figures S15G–S15I). These data, in combination with the low cytotoxicity (Figure S8C), slow clearance (Figure S10), non-aggregation behavior, and high SWIR brightness in aqueous solutions (Figures 2A, 2D, 2E, and S4), make **AmmonChrom7** a great candidate for cell-tracking experiments.

To showcase the excellent retention of **AmmonChrom7** in cell-tracking experiments, we monitored the *in vivo* growth of xenograft tumors in mice. We first stained A375 cells with 50 μM **AmmonChrom7** for 18 h prior to subcutaneous (*s.c.*) injection into the left flank of mice to track their growth as xenograft tumors (Figure 4A), with non-stained cells injected into the right flank as a control. The stained cells initially showed spread out and smeared fluorescent distribution upon injection (Figures 4C and S16A) and then became coagulated within the first 2 weeks, corresponding to the assimilation of Matrigel that initially supported the cells (Figures 4C and S16B). In the meantime, the brightness of the stained tumor increased corresponding to the increased dye density, allowing for image capturing with as short as 1 ms exposure time (Figure S16G). As the cells started to divide, the size of the fluorescence area gradually increased, which correlates well with the caliper measurement (Figure 4C). Although the overall mean fluorescence decreased upon tumor growth due to the dilution of the dye (Figure S16G), some regions of the tumor showed lower signals (Figures 4D, S16C, and S16D), possibly as indicators of actively growing sites versus more senescent locations of the tumor. Notably, the fluorescence signal was well-contained at tumor sites as seen in the bright-field image (Figures 4D and S16B–S16D). We then sacrificed the mice at varying time points depending on the size of the two tumors to obtain *ex vivo* images. As expected, the three stained tumors all showed bright fluorescence under a SWIR camera, whereas we observed much lower fluorescence in the surrounding tissue, negligible intensity in the liver, and essentially no fluorescence in the control tumors and the rest of the body (Figures 4E–4G). These results further confirm that **AmmonChrom7** was contained at the tumor site with minimal leakage. Additionally, the 3/3 take rate and comparable growing speed (Figure S16H) suggest that **AmmonChrom7** does not impact A375 tumor growth.

Next, we performed a similar experiment with the more challenging, slow-growing, xenograft model SK-OV-3. We treated SK-OV-3 cells with 50 μM **AmmonChrom7** prior to *s.c.* injection in the flank and abdomen of three mice. Again, the fluorescence signal showed clear overlap with the tumor location from bright-field images (Figures S17A and S17B). The size of the tumors remained largely unchanged since week 1, and the fluorescence intensity fluctuated accordingly, rather than decreasing (Figures S17D–S17F), suggesting that the dye was retained at the tumor site with little diffusion or degradation over the 38-day period. To our knowledge, this sets the record for the longest time period for a small-molecule SWIR dye to be monitored *in vivo*. To confirm that the fluorescence originated from the tumor, we injected the live mice intravenously with OTL-38, a recently FDA-approved NIR dye that labels the folate receptor[51] modestly expressed on SK-OV-3 cells. OTL-38 contains a NIR heptamethine analogous

to ICG as the fluorophore core, and thus, we envisioned that the tail emission in the SWIR could be utilized for imaging (Figure S17C). As expected, clear colocalization was observed in *in vivo* images (Figures S17A and S17B) and *ex vivo* images (Figure 4H), supporting that the dye continuously labels the SK-OV-3 tumor throughout the period of the experiment. Although non-specific accumulation of OTL-38 was observed in other organs, **AmmonChrom7** showed clear staining of the tumor with very little diffusion into the surrounding tissue (Figures 4H, 4I, and S17G–S17I), highlighting the cell-tracking potential of **AmmonChrom7**. Taken together, these experiments demonstrate that by incorporating multiple positive charges onto our dye scaffold, we successfully engineered **AmmonChrom7** as a cellular stain for the long-term tracking of tumor growth, offering the first small-molecule option for *in vivo* cell tracking using SWIR imaging. The high brightness and minimal cell growth inhibition provide a valuable tool for studying cancer models, as well as potential use in stem cell and immune cell research.

Targeted imaging with water-soluble SWIR fluorophores

Initially, we focused on appending functionality to **PropChrom7** that would induce water solubility; however, a major advantage of **PropChrom7** is the versatility of functionality that can be appended onto the SWIR chromophore. To showcase this, we prepared **11** (**PhosphoChrom7**) for bone-targeted imaging (Figure 5A). Four phosphate groups were clicked onto **PropChrom7** in 20% yield with the phosphate groups playing a dual role of hydrophilicity and Ca^{2+}-binding moieties. The unique binding affinity of phosphonates toward divalent metals has previously been harnessed in the development of bone-targeting drugs[52] and NIR bone imaging agents.[53–55] We thus anticipated that **PhosphoChrom7**, with its four phosphonates, could be delivered without a carrier and facilitate skeleton imaging due to its affinity for bone.

We first analyzed **PhosphoChrom7** in *in vitro* assays. The solubility of this compound in FBS is lower than the **Sulfo-**, **Ammon-**, or **Zwit-Chrom7** (Figure S18), which is consistent with trends seen for bisphosphonate drugs. The photophysical consequences of the decreased solubility are a broad absorption peak at 760 nm. Interestingly, this peak is independent of concentration in terms of relative intensity and is significantly blue-shifted compared with the other three water-soluble dyes, suggesting a different mode of variation from monomeric polymethine structure (Figures 5B and S18). Conversely, the absorption/emission wavelengths of the monomer peak are almost identical to the other three dyes (Figures 5B and S8A), providing further evidence that the functionality attached to **PropChrom7** does not drastically affect the photophysical properties of the monomeric fluorophore core.

We tested the binding affinity toward hydroxyapatite, the major mineral component of bone. Incubation with **PhosphoChrom7** in bovine serum led to a bright suspension of the particles under a SWIR camera, and most importantly, sequential washes with bovine serum only slightly decreased the overall brightness, indicating strong binding affinity of **PhosphoChrom7** toward hydroxyapatite (Figure 5C). To rule out the possibility of co-precipitation of the dye with the hydroxyapatite powder due to its limited solubility, we performed scanning electron microscopy on the particles. Although we were unable to observe standalone particles without calcium and phosphorus after dye-treatment, we detected a significant increase of carbon elements in energy-dispersive X-ray spectrometry (EDS) mapping for the dye-treated particles compared with untreated ones (Figure S19), suggesting that the dye was indeed adsorbed onto the calcium salt. The toxicity of
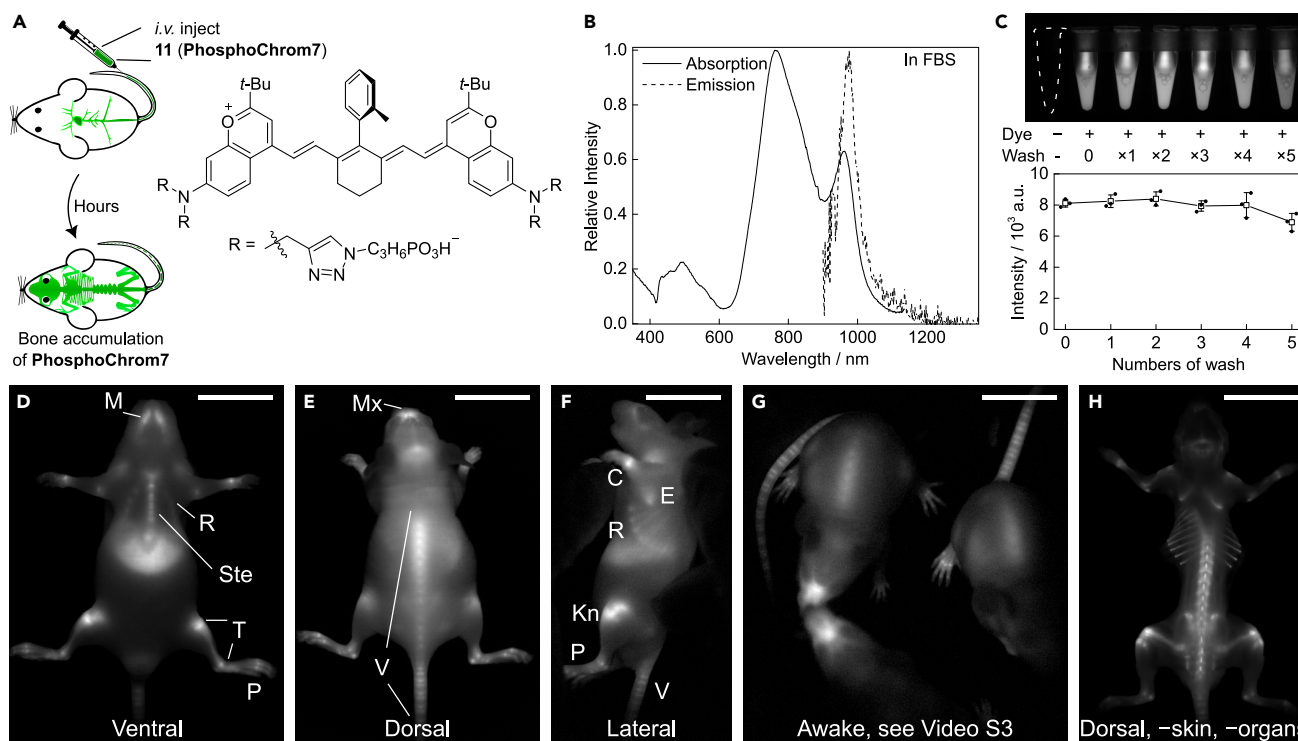
Figure 5. Imaging of bone using PhosphoChrom7

(A) Schematics of bone imaging by *s.c.* injection of **PhosphoChrom7**.

(B) Absorption and emission spectra of 2 μM **PhosphoChrom7** in FBS.

(C) Fluorescent image of calcium hydroxyapatite suspension in bovine serum treated with **PhosphoChrom7**, and its subsequent washes with bovine serum (0.5 ms/frame, 101 frames averaged, max brightness 11,338); quantification is shown below (mean ± SD, n = 3).

(D–F) Fluorescence images of a mouse 24 h after *i.v.* injection of 20 nmol **PhosphoChrom7** on (D) ventral, (E) dorsal, or (F) lateral view. M, mandible; Mx, maxilla; R, Rib; Ste, sternum; T, tibia; P, phalange; V, vertebrae; C, carpus; E, elbow; Kn, knee.

(G) Representative single frame from Video S3 showing fluorescence image of awake mice 48 h after injection.

(H) Fluorescence images of a mouse after removal of abdominal organs and most of the skin on dorsal view. Images were captured under 100 mW/cm^2 975 nm illumination at 3 ms/frame (D–H); 81 frames (D and E), single frame (F and G), or 201 frames (H) averaged. Max brightness: 7,096 (D), 4,985 (E), 6,379 (F), 6,962 (G), and 12,313 (H). Scale bars: 2 cm.

PhosphoChrom7 is also mild at low concentrations (Figure S8C), similar to **Sulfo-** and **Zwit-Chrom7**. Collectively, these properties of **PhosphoChrom7** meet the criteria for bone-targeted SWIR imaging.

We then performed mouse imaging using the tetraphosphonate SWIR fluorophore **PhosphoChrom7**. After intravenous (*i.v.*) injection, **PhosphoChrom7** initially localized in the vasculature (Figures S20A and S20F) but gradually redistributed and began to feature bone structures at 8 h (Figures S20B and S20G), along with some accumulation in the liver. Aside from strong liver staining, the reduction of non-bone-localized signals gave rise to a contour of mouse skeleton after 24 or 48 h (Figures 5D–5F, S20C, S20D, S20H, and S20I) with slightly faster clearance compared with previous hydrophilic dyes (Figures S20N and S20O). Although the dye may localize more onto bone regions with higher osteoblast or circulation activity, the SWIR image clearly outlines the mandible, sternum, tibia, and phalange bones on the ventral view (Figure 5D) and maxilla and vertebra on the dorsal side (Figure 5E). The rib cage can be clearly visualized on the lateral view when the skin is gently lifted around the shoulder to reduce scattering (Figure 5F). The high brightness of **PhosphoChrom7** also enables bone imaging in awake and moving mice with comparable details (Figure 5G; Video S3). Most importantly, all these

Table 1. Summary of the photophysical properties of water-soluble bioconjugates from PropChrom7

Azide	Product	Solvent	$\lambda_{max, abs}$/nm	$\lambda_{max, ems}$/nm	φ_F
cRGD-N$_3$	**cRGD-Chrom7**	MeOH	945	961	0.0060
		FBS	968	969	0.0030
GalNAc-PEG-N$_3$	**GalNAc-Chrom7**	MeOH	944	963	0.0080
		FBS	960	965	0.0030
Lys(N$_3$)-KKEEE	**KKEEE-Chrom7**	MeOH	941	957	0.0100
		FBS	964	969	0.0040

See Figure S21B for structures and error values.

features were readily identifiable with high resolution in living mice without skin removal. However, when the skin was removed from the mouse carcass, more details of its bone structure were revealed (Figures S20E and S20J). Images of the dissected organs indicate that although bone was clearly stained by **Phospho-Chrom7**, the liver is the major target of the dye similar to our other hydrophilic dyes described herein (Figures S20L and S20M). We further removed the abdominal organs to eliminate their interference and were able to obtain a high-contrast image of the skeleton of the mouse (Figures 5H and S20K). By facile introduction of calcium-binding phosphonates to our tetravalent functionalization platform, **PhosphoChrom7** stands out as the first reported bone-targeting SWIR fluorophore. **PhosphoChrom7** enables non-invasive optical imaging of bone at video-rate speeds, providing a platform for studying osteology and bone-related diseases in model animals.

We finally sought to investigate the possibility of targeted imaging by introducing small and hydrophilic biomolecules with well-defined bioactivities. Against this backdrop, we selected cyclic Arg-Gly-Asp (cRGD) azide as a peptide that is widely used for targeting $\alpha_v\beta_3$ integrin seen in tumor angionesis,[56,57] kidney-localizing peptide Lys-Lys-Glu-Glu-Glu (KKEEE) azide with affinity toward proximal tubule cells,[58,59] and N-Acetylgalactosamine (GalNAc) azide as a monosaccharide for selective liver delivery.[60] We hereby synthesized the targeted conjugates, namely **cRGD-Chrom7**, **GalNAc-Chrom7**, and **KKEEE-Chrom7**, from **PropChrom7** via single-step CuAAC, and were able to separate the products in an analogous manner (Figure S21A). All of these dyes readily dissolve in methanol as monomeric species with SWIR emission (Figure S21) and show absorption and emission maxima similar to all aforementioned dyes in MeOH and FBS (Table 1; Figures S21 and S22). These additional examples showcase the wide applicability of our platform with **PropChrom7** as a central intermediate for the facile generation of hydrophilic SWIR fluorophores for vasculature contrast, cell tracking, and molecular imaging.

Concluding remarks

To close, we have reported a modular platform that uses **PropChrom7** as a central intermediate with four conjugation handles to easily access a series of functionalized SWIR fluorophores via CuAAC. Through this platform, we obtained **Sulfo-**, **Ammon-**, **Zwit-**, **Phospho-Chrom7**, and several **Chrom7** bioconjugates as hydrophilic/water-soluble SWIR dyes. All these dyes display minimal aggregation and ground-state desymmetrization in serum. They also exhibit bright SWIR fluorescence when *i.v.* injected in mice and can be imaged with video-frame rates. Notably, these dyes readily dissolve in buffer as homogeneous solutions for convenient, direct

administration, without concerns of batch variation, storage instability, or potential *in vivo* breakdown, which are frequently encountered for micelle formulations.

Besides the increased hydrophilicity imparted by the late-stage click reaction, this family of SWIR fluorophores offers versatile imaging tools. In particular, the anionic dye **SulfoChrom7** stands out as a red-shifted analog of **ICG** with greatly enhanced SWIR brightness and longer circulation time. **SulfoChrom7** facilitates imaging of mouse liver and vasculature with as little as 0.05 nmol, the smallest amount reported of contrast agents that enabled video-rate imaging. The cationic dye **AmmonChrom7** enables the monitoring of xenograft tumor growth over weeks with minimal signal loss and little diffusion into other tissues owing to its excellent brightness, biocompatibility, *in vivo* stability, and cellular retention. Our tumor-tracking experiments also set the record of *in vivo* detection time length for SWIR dyes. The cell-tracking capability of this dye has the potential for use in monitoring cell activities in *in vivo* studies on tumorigenesis and immune cell migration. Finally, **PhosphoChrom7** exhibits strong binding to calcium minerals due to the four phosphonate groups on the molecule, furnishing the first bone-targeting fluorophore in the SWIR. Its brightness and reduced scattering of SWIR light eliminate the need for sacrificing, skinning, or even anesthesia of the mice for bone imaging, enabling non-invasive video recording of the skeleton in awake, moving mice.

Our design also serves as a starting point for the modular design of water-soluble, functional, and carrier-free SWIR fluorophores for *in vivo* imaging. By separating the fluorophore synthesis and the introduction of water solubility and/or bioactivity, this late-stage modification method allows for the facile combination of the fluorophore core and various functional groups tailored toward specific imaging requirements without worries about the functional group compatibilities and tedious aqueous purification during the synthesis of the fluorophore core. Although our current tetravalent modification is expected to enhance targeting through avidity, it is also beneficial to explore other topology choices such as four water-solubilization groups and a single bioactive moiety. Our group is currently expanding the scope of both the packaged fluorophore core and other hydrophilic/bioactive functionalities to extend the platform for targeted and formulation-free SWIR imaging, with an overarching goal of providing user-friendly building blocks of SWIR detection reagents similar to the success of many commercially available activated fluorophores in the visible region for easy bioconjugation. Finally, the reported fluorophore functionalization through bispropargylation of aniline groups also provides a method for the future development of other aniline-containing molecules as modularized imaging agents and, more broadly, as other chemical biology tools.

EXPERIMENTAL PROCEDURES

See supplemental experimental procedures for detailed procedures and characterization methods.

Resource availability
Lead contact
Further information and requests for resources and reagents should be directed to and will be fulfilled by the lead contact, Ellen M. Sletten (sletten@chem.ucla.edu).

Materials availability
New fluorophores in this study will be made available on request, but we may require a payment and/or a completed materials transfer agreement if there is potential for commercial application.

Code availability

This paper does not involve original code.

Data and code availability

Raw and processed imaging files for the figures in this paper is available through BioImage Archive (accession number: S-BIAD841). Any additional information required to reanalyze the data reported in this paper is available from the lead contact upon request.

SUPPLEMENTAL INFORMATION

Supplemental information can be found online at https://doi.org/10.1016/j.chempr.2023.08.021.

AUTHOR CONTRIBUTIONS

E.M.S. conceived and supervised the project. E.M.S. and J.S. designed the experiments. J.S. carried out the synthesis and *in vitro* characterization of compounds **1**– **11**. E.Y.L. performed additional *in vitro* characterization. E.B.M. and E.Y.L optimized the synthetic procedures, synthesized, and characterized **7′**, **8′** and the rest of the fluorophores. L.G. performed electron microscopy assays on PhosphoChrom7. P.S.L. and S.K. contributed OTL-38. J.S., I.L., and E.Y.L. performed *in vivo* operation and imaging of the fluorophores. E.M.S. and J.S. wrote the manuscript draft. All authors contributed to the review and editing of the paper.

DECLARATION OF INTERESTS

Work in this report is included in patent PCT/US2023/062095. P.S.L. is employed by Purdue University, which owns the patents for OTL-38.

INCLUSION AND DIVERSITY

We support inclusive, diverse, and equitable conduct of research.

REFERENCES

1. Hong, G., Antaris, A.L., and Dai, H. (2017). Near-infrared fluorophores for biomedical imaging. Nat. Biomed. Eng. *1*, 1–22. https://doi.org/10.1038/s41551-016-0010.

2. Thimsen, E., Sadtler, B., and Berezin, M.Y. (2017). Shortwave-infrared (SWIR) emitters for biological imaging: a review of challenges and opportunities. Nanophotonics *6*, 1043–1054. https://doi.org/10.1515/nanoph-2017-0039.

3. Li, C., Chen, G., Zhang, Y., Wu, F., and Wang, Q. (2020). Advanced fluorescence imaging technology in the near-infrared-II window for biomedical applications. J. Am. Chem. Soc. *142*, 14789–14804. https://doi.org/10.1021/jacs.0c07022.

4. Lim, Y.T., Kim, S., Nakayama, A., Stott, N.E., Bawendi, M.G., and Frangioni, J.V. (2003). Selection of quantum dot wavelengths for biomedical assays and imaging. Mol. Imaging *2*, 50–64. https://doi.org/10.1162/15353500200302163.

5. Diao, S., Hong, G., Antaris, A.L., Blackburn, J.L., Cheng, K., Cheng, Z., and Dai, H. (2015). Biological imaging without autofluorescence in the second near-infrared region. Nano Res. *8*, 3027–3034. https://doi.org/10.1007/s12274-015-0808-9.

6. Del Rosal, B., Villa, I., Jaque, D., and Sanz-Rodríguez, F. (2016). In vivo autofluorescence in the biological windows: the role of

pigmentation. J. Biophotonics *9*, 1059–1067. https://doi.org/10.1002/jbio.201500271.

7. Schnermann, M.J. (2017). Chemical biology: organic dyes for deep bioimaging. Nature *551*, 176–177. https://doi.org/10.1038/nature24755.

8. Welsher, K., Liu, Z., Sherlock, S.P., Robinson, J.T., Chen, Z., Daranciang, D., and Dai, H. (2009). A route to brightly fluorescent carbon nanotubes for near-infrared imaging in mice. Nat. Nanotechnol. *4*, 773–780. https://doi.org/10.1038/nnano.2009.294.

9. Hu, Z., Fang, C., Li, B., Zhang, Z., Cao, C., Cai, M., Su, S., Sun, X., Shi, X., Li, C., et al. (2020). First-in-human liver-tumour surgery guided by multispectral fluorescence imaging in the visible and near-infrared-I/II windows. Nat. Biomed. Eng. *4*, 259–271. https://doi.org/10.1038/s41551-019-0494-0.

10. Grimm, J.B., and Lavis, L.D. (2022). Caveat fluorophore: an insiders' guide to small-molecule fluorescent labels. Nat. Methods *19*, 149–158. https://doi.org/10.1038/s41592-021-01338-6.

11. Choi, H.S., Gibbs, S.L., Lee, J.H., Kim, S.H., Ashitate, Y., Liu, F., Hyun, H., Park, G., Xie, Y., Bae, S., et al. (2013). Targeted zwitterionic near-infrared fluorophores for improved optical imaging. Nat. Biotechnol. *31*, 148–153. https://doi.org/10.1038/nbt.2468.

12. Bricks, J.L., Kachkovskii, A.D., Slominskii, Y.L., Gerasov, A.O., and Popov, S.V. (2015). Molecular design of near infrared polymethine dyes: a review. Dyes Pigm. *121*, 238–255. https://doi.org/10.1016/j.dyepig.2015.05.016.

13. Tatikolov, A.S. (2012). Polymethine dyes as spectral-fluorescent probes for biomacromolecules. J. Photochem. Photobiol. C *13*, 55–90. https://doi.org/10.1016/j.jphotochemrev.2011.11.001.

14. Gorka, A.P., Nani, R.R., and Schnermann, M.J. (2015). Cyanine polyene reactivity: scope and biomedical applications. Org. Biomol. Chem. *13*, 7584–7598. https://doi.org/10.1039/c5ob00788g.

15. Ma, X., Shi, L., Zhang, B., Liu, L., Fu, Y., and Zhang, X. (2022). Recent advances in bioprobes and biolabels based on cyanine dyes. Anal. Bioanal. Chem. *414*, 4551–4573. https://doi.org/10.1007/s00216-022-03995-8.

16. Swamy, M.M.M., Murai, Y., Monde, K., Tsuboi, S., and Jin, T. (2021). Shortwave-infrared fluorescent molecular imaging probes based on π-conjugation extended indocyanine green. Bioconjug. Chem. *32*, 1541–1547. https://doi.org/10.1021/acs.bioconjchem.1c00253.

17. Bandi, V.G., Luciano, M.P., Saccomano, M., Patel, N.L., Bischof, T.S., Lingg, J.G.P., Tsrunchev, P.T., Nix, M.N., Ruehle, B., Sanders, C., et al. (2022). Targeted multicolor in vivo imaging over 1,000 nm enabled by nonamethine cyanines. Nat. Methods *19*, 353–358. https://doi.org/10.1038/s41592-022-01394-6.

18. Zhu, S., Tian, R., Antaris, A.L., Chen, X., and Dai, H. (2019). Near-infrared-II molecular dyes for cancer imaging and surgery. Adv. Mater. *31*, e1900321. https://doi.org/10.1002/adma.201900321.

19. Lei, Z., and Zhang, F. (2021). Molecular engineering of NIR-II fluorophores for improved biomedical detection. Angew. Chem. Int. Ed. Engl. *60*, 16294–16308. https://doi.org/10.1002/anie.202007040.

20. Wong, K.C.Y., and Sletten, E.M. (2022). Extending optical chemical tools and technologies to mice by shifting to the shortwave infrared region. Curr. Opin. Chem. Biol. *68*, 102131. https://doi.org/10.1016/j.cbpa.2022.102131.

21. Tolbert, L.M., and Zhao, X. (1997). Beyond the cyanine limit: Peierls distortion and symmetry collapse in a polymethine dye. J. Am. Chem. Soc. *119*, 3253–3258. https://doi.org/10.1021/ja9626953.

22. Terenziani, F., Przhonska, O.V., Webster, S., Padilha, L.A., Slominsky, Y.L., Davydenko, I.G., Gerasov, A.O., Kovtun, Y.P., Shandura, M.P., Kachkovski, A.D., et al. (2010). Essential-state model for polymethine dyes: symmetry breaking and optical spectra. J. Phys. Chem. Lett. *1*, 1800–1804. https://doi.org/10.1021/jz100430x.

23. Li, B., Lu, L., Zhao, M., Lei, Z., and Zhang, F. (2018). An efficient 1064 nm NIR-II excitation fluorescent molecular dye for deep-tissue high-resolution dynamic bioimaging. Angew. Chem. Int. Ed. Engl. *57*, 7483–7487. https://doi.org/10.1002/anie.201801226.

24. Li, B., Zhao, M., Feng, L., Dou, C., Ding, S., Zhou, G., Lu, L., Zhang, H., Chen, F., Li, X., et al. (2020). Organic NIR-II molecule with long blood half-life for in vivo dynamic vascular imaging. Nat. Commun. *11*, 3102. https://doi.org/10.1038/s41467-020-16924-z.

25. Cosco, E.D., Caram, J.R., Bruns, O.T., Franke, D., Day, R.A., Farr, E.P., Bawendi, M.G., and Sletten, E.M. (2017). Flavylium polymethine fluorophores for near- and shortwave infrared imaging. Angew. Chem. Int. Ed. Engl. *56*, 13126–13129. https://doi.org/10.1002/anie.201706974.

26. Cosco, E.D., Spearman, A.L., Ramakrishnan, S., Lingg, J.G.P., Saccomano, M., Pengshung, M., Arús, B.A., Wong, K.C.Y., Glasl, S., Ntziachristos, V., et al. (2020). Shortwave infrared polymethine fluorophores matched to excitation lasers enable non-invasive, multicolour in vivo imaging in real time. Nat. Chem. *12*, 1123–1130. https://doi.org/10.1038/s41557-020-00554-5.

27. Cosco, E.D., Arús, B.A., Spearman, A.L., Atallah, T.L., Lim, I., Leland, O.S., Caram, J.R., Bischof, T.S., Bruns, O.T., and Sletten, E.M. (2021). Bright chromenylium polymethine dyes enable fast, four-color in vivo imaging with shortwave infrared detection. J. Am. Chem. Soc. *143*, 6836–6846. https://doi.org/10.1021/jacs.0c11599.

28. Pengshung, M., Li, J., Mukadum, F., Lopez, S.A., and Sletten, E.M. (2020). Photophysical tuning of shortwave infrared flavylium heptamethine dyes via substituent placement. Org. Lett. *22*, 6150–6154. https://doi.org/10.1021/acs.orglett.0c02213.

29. Wang, S., Fan, Y., Li, D., Sun, C., Lei, Z., Lu, L., Wang, T., and Zhang, F. (2019). Anti-quenching NIR-II molecular fluorophores for in vivo high-contrast imaging and pH sensing. Nat.

Commun. *10*, 1058. https://doi.org/10.1038/s41467-019-09043-x.

30. Lei, Z., Sun, C., Pei, P., Wang, S., Li, D., Zhang, X., and Zhang, F. (2019). Stable, wavelength-tunable fluorescent dyes in the NIR-II region for in vivo high-contrast bioimaging and multiplexed biosensing. Angew. Chem. Int. Ed. Engl. *58*, 8166–8171. https://doi.org/10.1002/anie.201904182.

31. He, Y., Wang, S., Yu, P., Yan, K., Ming, J., Yao, C., He, Z., El-Toni, A.M., Khan, A., Zhu, X., et al. (2021). NIR-II cell endocytosis-activated fluorescent probes for in vivo high-contrast bioimaging diagnostics. Chem. Sci. *12*, 10474–10482. https://doi.org/10.1039/D1SC02763H.

32. Urano, Y., Kamiya, M., Kanda, K., Ueno, T., Hirose, K., and Nagano, T. (2005). Evolution of fluorescein as a platform for finely tunable fluorescence probes. J. Am. Chem. Soc. *127*, 4888–4894. https://doi.org/10.1021/ja043919h.

33. Seijas, J.A., Vázquez-Tato, M.P., and Carballido-Reboredo, R. (2005). Solvent-free synthesis of functionalized flavones under microwave irradiation. J. Org. Chem. *70*, 2855–2858. https://doi.org/10.1021/jo048685z.

34. Lee, H., Mason, J.C., and Achilefu, S. (2006). Heptamethine cyanine dyes with a robust C−C bond at the central position of the chromophore. J. Org. Chem. *71*, 7862–7865. https://doi.org/10.1021/jo061284u.

35. Hong, V., Presolski, S.I., Ma, C., and Finn, M.G. (2009). Analysis and optimization of copper-catalyzed azide–alkyne cycloaddition for bioconjugation. Angew. Chem. Int. Ed. Engl. *48*, 9879–9883. https://doi.org/10.1002/anie.200905087.

36. Cosco, E.D., Lim, I., and Sletten, E.M. (2021). Photophysical properties of indocyanine green in the shortwave infrared region. ChemPhotoChem *5*, 727–734. https://doi.org/10.1002/cptc.202100045.

37. Aharoni, A., Oron, D., Banin, U., Rabani, E., and Jortner, J. (2008). Long-range electronic-to-vibrational energy transfer from nanocrystals to their surrounding matrix environment. Phys. Rev. Lett. *100*, 057404. https://doi.org/10.1103/PhysRevLett.100.057404.

38. Maillard, J., Klehs, K., Rumble, C., Vauthey, E., Heilemann, M., and Fürstenberg, A. (2020). Universal quenching of common fluorescent probes by water and alcohols. Chem. Sci. *12*, 1352–1362. https://doi.org/10.1039/D0SC05431C.

39. Gathje, J., Steuer, R.R., and Nicholes, K.R. (1970). Stability studies on indocyanine green dye. J. Appl. Physiol. *29*, 181–185. https://doi.org/10.1152/jappl.1970.29.2.181.

40. Mindt, S., Karampinis, I., John, M., Neumaier, M., and Nowak, K. (2018). Stability and degradation of indocyanine green in plasma, aqueous solution and whole blood. Photochem. Photobiol. Sci. *17*, 1189–1196. https://doi.org/10.1039/C8PP00064F.

41. Li, D.H., Gamage, R.S., and Smith, B.D. (2022). Sterically shielded hydrophilic analogs of indocyanine green. J. Org. Chem. *87*, 11593–11601. https://doi.org/10.1021/acs.joc.2c01229.

42. Orrenius, S., and Moldéus, P. (1984). The multiple roles of glutathione in drug metabolism. Trends Pharmacol. Sci. *5*, 432–435. https://doi.org/10.1016/0165-6147(84)90495-4.

43. Milesi-Hallé, A., Abdel-Rahman, S.M., Brown, A., McCullough, S.S., Letzig, L., Hinson, J.A., and James, L.P. (2011). Indocyanine green clearance varies as a function of N-acetylcysteine treatment in a murine model of acetaminophen toxicity. Chem. Biol. Interact. *189*, 222–229. https://doi.org/10.1016/j.cbi.2010.12.001.

44. Carr, J.A., Franke, D., Caram, J.R., Perkinson, C.F., Saif, M., Askoxylakis, V., Datta, M., Fukumura, D., Jain, R.K., Bawendi, M.G., et al. (2018). Shortwave infrared fluorescence imaging with the clinically approved near-infrared dye indocyanine green. Proc. Natl. Acad. Sci. USA *115*, 4465–4470. https://doi.org/10.1073/pnas.1718917115.

45. van Manen, L., Handgraaf, H.J.M., Diana, M., Dijkstra, J., Ishizawa, T., Vahrmeijer, A.L., and Mieog, J.S.D. (2018). A practical guide for the use of indocyanine green and methylene blue in fluorescence-guided abdominal surgery. J. Surg. Oncol. *118*, 283–300. https://doi.org/10.1002/jso.25105.

46. Gao, S., Yu, Y., Wang, Z., Wu, Y., Qiu, X., Jian, C., and Yu, A. (2022). NIR-II fluorescence imaging using indocyanine green provides early prediction of skin avulsion-injury in a porcine model. Clin. Cosmet. Investig. Dermatol. *15*, 447–454. https://doi.org/10.2147/CCID.S357989.

47. Carr, J.A., Aellen, M., Franke, D., So, P.T.C., Bruns, O.T., and Bawendi, M.G. (2018). Absorption by water increases fluorescence image contrast of biological tissue in the shortwave infrared. Proc. Natl. Acad. Sci. USA *115*, 9080–9085. https://doi.org/10.1073/pnas.1803210115.

48. Dhaliwal, K., Escher, G., Unciti-Broceta, A., McDonald, N., Simpson, A.J., Haslett, C., and Bradley, M. (2011). Far red and NIR dye-peptoid conjugates for efficient immune cell labelling and tracking in preclinical models. MedChemComm *2*, 1050–1053. https://doi.org/10.1039/C1MD00171J.

49. Wang, L., Xia, Q., Hou, M., Yan, C., Xu, Y., Qu, J., and Liu, R. (2017). A photostable cationic fluorophore for long-term bioimaging. J. Mater. Chem. B *5*, 9183–9188. https://doi.org/10.1039/C7TB02668D.

50. Chen, G., Zhang, Y., Li, C., Huang, D., Wang, Q., and Wang, Q. (2018). Recent advances in tracking the transplanted stem cells using near-infrared fluorescent Nanoprobes: turning from the first to the second near-infrared window. Adv. Healthc. Mater. *7*, e1800497. https://doi.org/10.1002/adhm.201800497.

51. Mahalingam, S.M., Kularatne, S.A., Myers, C.H., Gagare, P., Norshi, M., Liu, X., Singhal, S., and Low, P.S. (2018). Evaluation of novel tumor-targeted near-infrared probe for fluorescence-guided surgery of cancer. J. Med. Chem. *61*, 9637–9646. https://doi.org/10.1021/acs.jmedchem.8b01115.

52. McClung, M., Harris, S.T., Miller, P.D., Bauer, D.C., Davison, K.S., Dian, L., Hanley, D.A., Kendler, D.L., Yuen, C.K., and Lewiecki, E.M. (2013). Bisphosphonate therapy for osteoporosis: benefits, risks, and drug holiday. Am. J. Med. *126*, 13–20. https://doi.org/10.1016/j.amjmed.2012.06.023.

53. Zaheer, A., Lenkinski, R.E., Mahmood, A., Jones, A.G., Cantley, L.C., and Frangioni, J.V. (2001). In vivo near-infrared fluorescence imaging of osteoblastic activity. Nat. Biotechnol. *19*, 1148–1154. https://doi.org/10.1038/nbt1201-1148.

54. Bhushan, K.R., Misra, P., Liu, F., Mathur, S., Lenkinski, R.E., and Frangioni, J.V. (2008). Detection of breast cancer microcalcifications using a dual-modality SPECT/NIR fluorescent probe. J. Am. Chem. Soc. *130*, 17648–17649. https://doi.org/10.1021/ja807099s.

55. Hyun, H., Wada, H., Bao, K., Gravier, J., Yadav, Y., Laramie, M., Henary, M., Frangioni, J.V., and Choi, H.S. (2014). Phosphonated near-infrared fluorophores for biomedical imaging of bone. Angew. Chem. Int. Ed. Engl. *53*, 10668–10672. https://doi.org/10.1002/anie.201404930.

56. Danhier, F., Le Breton, A., and Préat, V. (2012). RGD-based strategies to target alpha(v) beta(3) integrin in cancer therapy and diagnosis. Mol. Pharm. *9*, 2961–2973. https://doi.org/10.1021/mp3002733.

57. Asati, S., Pandey, V., and Soni, V. (2019). RGD peptide as a targeting moiety for theranostic purpose: an update study. Int. J. Pept. Res. Ther. *25*, 49–65. https://doi.org/10.1007/s10989-018-9728-3.

58. Wischnjow, A., Sarko, D., Janzer, M., Kaufman, C., Beijer, B., Brings, S., Haberkorn, U., Larbig, G., Kübelbeck, A., and Mier, W. (2016). Renal targeting: peptide-based drug delivery to proximal tubule cells. Bioconjug. Chem. *27*, 1050–1057. https://doi.org/10.1021/acs.bioconjchem.6b00057.

59. Janzer, M., Larbig, G., Kübelbeck, A., Wischnjow, A., Haberkorn, U., and Mier, W. (2016). Drug conjugation affects pharmacokinetics and specificity of kidney-targeted peptide carriers. Bioconjug. Chem. *27*, 2441–2449. https://doi.org/10.1021/acs.bioconjchem.6b00397.

60. Debacker, A.J., Voutila, J., Catley, M., Blakey, D., and Habib, N. (2020). Delivery of oligonucleotides to the liver with GalNAc: from research to registered therapeutic drug. Mol. Ther. *28*, 1759–1771. https://doi.org/10.1016/j.ymthe.2020.06.015.